PCCP

PAPER

View Article Online
View Journal | View Issue

Cite this: *Phys. Chem. Chem. Phys.*, 2019, **21**, 15062

Water diffusion measurements of single charged aerosols using H_2O/D_2O isotope exchange and Raman spectroscopy in an electrodynamic balance†

Katherine A. Nadler, Pyeongeun Kim, Dao-Ling Huang, Wei Xiong and Robert E. Continetti *

Received 14th November 2018,
Accepted 10th June 2019

DOI: 10.1039/c8cp07052k

rsc.li/pccp

Sea spray aerosols contain a large array of organic compounds that contribute to high viscosities at low relative humidity and temperature thereby slowing translational diffusion of water. The Stokes–Einstein equation describes how viscosity is inversely correlated with the translational diffusion coefficient of the diffusing species. However, recent studies indicate that the Stokes–Einstein equation breaks down at high viscosities achieved in the particle phase ($>10^{12}$ Pa s), underestimating the predicted water diffusion coefficient by orders of magnitude and revealing the need for directly studying the diffusion of water in single aerosols. A new method is reported for measuring the water diffusion coefficient in single suspended charged sucrose–water and citric acid (CA)–water microdroplets in the 30–60 micron diameter range. The translational water diffusion coefficient is quantified using the H_2O/D_2O isotope exchange technique between 26 and 54% relative humidity (RH) for sucrose and 7 and 25% RH for CA using a recently developed mobile electrodynamic balance apparatus. The results are in good agreement with the literature, particularly the Vignes-type parameterization from experiments using isotope exchange and optical tweezers. Below 15% RH, CA droplets show incomplete H_2O/D_2O exchange. This mobile electrodynamic balance will allow future studies of atmospherically relevant chemical systems, including field studies.

1 Introduction

Atmospheric aerosols are capable of scattering and absorbing solar radiation directly as well as interacting indirectly through cloud formation, and thus they have great impact on climate and the hydrological cycle. Recently, the discovery of highly viscous and amorphous biogenic aerosols[1,2] has attracted attention due to the prospect of very slow kinetics governing chemical change in these systems.[3–5] While aqueous droplets with low viscosities establish equilibrium with the surrounding environment rapidly, the reduced translational mobility of molecules in high viscosity droplets reduces the rate of equilibration. This inevitably leads to reductions in heterogeneous reaction rates,[6,7] impedes hygroscopic growth,[8–10] and enhances ice nucleation.[11,12] In order to quantify and model these phenomena, an understanding of water diffusion within such aerosol particles is essential as water is often the most mobile component in a viscous aqueous solution. This work presents a method for spectroscopically measuring water diffusion using isotope exchange in single model aerosols using an electrodynamic balance.

The Stokes–Einstein relation describes the diffusivity of solutes as a function of viscosity. A number of experimental techniques have been developed[4,13–15] to measure the viscosity of individual aerosol particles both in the field and in the laboratory. In particular, recent studies have examined the impact of chemical composition and oxidation state of a variety of organic compounds on viscosity spanning a dynamic range from 10^{-3} Pa s to values above the glass transition of 10^{12} Pa s.[16] Experimental techniques for measuring viscosity are important for improving our understanding of how chemical and environmental factors impact the phase state and heterogeneous reaction rates of ambient aerosols. Saccharides, in particular sucrose, have been used as model systems for validating new techniques to measure single aerosol viscosity[9,15] because they can undergo a change in viscosity of greater than 10 orders of magnitude between 0 and 100% RH, allowing for the comparison of methods over a wide dynamic range. Sea spray has been shown to contain a significant fraction of organic materials, particularly in the smaller size range ($d < 1$ μm).[17] Sucrose–water and CA–water can serve as benchmark systems to study the impacts of oxidized organic solute sea spray aerosols on varying RH. However, application of the Stokes–Einstein relationship to

Department of Chemistry and Biochemistry, University of California San Diego, 9500 Gilman Drive, La Jolla, California 92093-0340, USA.
E-mail: rcontinetti@ucsd.edu; Tel: +1-858-534-6402

† Electronic supplementary information (ESI) available. See DOI: 10.1039/c8cp07052k

aerosols using viscosity measurements alone has been shown to provide only a lower bound to the estimation of the diffusion coefficient because of the ability of water molecules to percolate through channels in viscous matrices.[16,18,19] Therefore, techniques that measure water diffusion independent from viscosity are necessary to accurately predict evaporation, condensation, and cloud activation processes.

The development of methods to measure slow water diffusion directly has been a challenge, and only in recent years have several complementary methods been reported. Zhu *et al.* quantified maltose diffusion using Raman microscopy and isotopic labeling by compressing a non-deuterated and deuterated drop of maltose between two glass slides, creating an interface between the droplets.[20] The Raman C–D and C–H stretches were used to monitor the diffusion of the molecules across the interface as a function of temperature and humidity. Price *et al.* extended the method of Zhu to measure the diffusion coefficient for water in a sucrose–water disk by isotopically labeling the gas phase molecules and monitoring the substitution of D_2O for H_2O in the solution *via* Raman microscopy.[21]

However, compared to studying water diffusion of atmospheric aerosols on a substrate, contactless single particle techniques are preferred, because the aerosol is free from impacts of surface perturbations at concentrations above the solubility limit. In addition, single particle measurements are preferred over ensemble-averaged experiments, because composition and local chemical environments vary from particle to particle. Optical tweezers are one technique for spectroscopic studies of single, spherical particles from 1–10 μm in diameter trapped at the center of a tightly focused laser beam by a balance of photon gradient forces that are insensitive to charge state.[22] Scattering from the focusing laser is collected to provide high resolution size measurements using cavity enhanced features of the light scattering such as morphology dependent resonances,[23,24] as well as chemical identity from the Raman scattering or fluorescence. The response of a single particle to changes in humidity or ambient gaseous composition provides measurements of chemical kinetics[25,26] and hygroscopicity.[27] For example, Davies *et al.* combined the isotopic exchange technique with an aerosol optical tweezer for single-particle confinement[28] allowing for a reduction in the sample size to less than 6 μm radius, speeding up the experimental timescales from weeks to hours. Isotopic tracer experiments have been carried out at a constant relative humidity (RH) leading to a constant size and solute concentration. Using Fick's second law of diffusion, Davies *et al.* modeled the time-dependent intensities of the ν(O–D) and ν(O–H) Raman peaks to quantify the diffusion coefficient as a function of concentration or water activity.[28]

The electrodynamic balance (EDB) is a single particle technique that offers similar advantages including contactless levitation. However, it is not limited by size or morphology, as the trapping potential depends solely on the mass-to-charge ratio. EDBs have been used extensively to measure physicochemical properties of single aerosol particles such as evaporation rates[29–32] and nucleation,[33–37] and provide complementary results to those obtained using optical tweezers. For example, Zobrist *et al.* used an EDB to conduct water diffusion measurements by creating a step change in the RH and observing the change in particle size *via* Mie resonance spectroscopy.[38] The result was interpreted using a theoretical framework based on principles of mass transport by dividing the particle into a discrete number of shells, within which water molecules translationally move to establish equilibrium. The flux of water molecules between shells, along with dynamic adjustment to the time-steps and shell thickness, was calculated to extract a concentration-dependent diffusion coefficient. Under high viscosity conditions, the particle was assumed to be in a core–shell phase state as the surface established equilibrium rapidly while the core remained viscous, creating a non-linear radial concentration gradient. This led to the refractive index becoming a fit parameter along with the radius, decreasing the accuracy of the model at low RH. Despite differences in experimental setups, the isotope tracing model and mass transport model produce similar water diffusion coefficients in sucrose over a wide range of RH.[21,28,38]

The present work reports a technique that combines the Raman spectroscopic isotope tracing method previously applied on single aerosols in optical tweezers by Davies *et al.*[28] with a RH-controlled EDB to trap single charged aerosol droplets for measuring water diffusion. Sucrose–H_2O and CA–H_2O microdroplets are serially trapped and equilibrated at a specific RH, and then exposed to D_2O at the same RH. Raman spectra of the droplet are acquired as a function of time, in order to assess the progression of D_2O diffusion into the droplet. In the analysis of these measurements, it is assumed that the entire droplet is irradiated with the laser and the total content of water remains constant throughout an experiment so that a volume-averaged Fickian diffusion model can be used to describe the exponential growth of the ν(O–D) Raman peak. In the case of sucrose, D_2O was observed to eventually replace all H_2O, as indicated by the complete disappearance of the ν(O–H) asymmetric stretch peak in the Raman spectrum. At RH below 10%, CA was not observed to completely exchange, indicating a kinetic limitation. In the following section, the experimental approach is described followed by presentation of the data for sucrose–water and CA–water.

2 Experimental

Water diffusion in single, charged aqueous microdroplets was studied using a D_2O/H_2O isotope exchange method in a new electrodynamic balance (EDB). Schematics of the experimental setup and optical layout are shown in Fig. 1. The geometry of the electrodynamic balance electrode is based on the design of Schlemmer *et al.*[39] later characterized in detail by Trevitt *et al.*[40] The balance is composed of two conical endcap electrodes separated by 5.3 mm with a 2.5 mm axial channel for laser optical access. Eight concentric rod electrodes replace the ring electrode in a traditional Paul trap, allowing for optical access over a wide range of angles. Each rod is electrically isolated, however an external DC levitation voltage is applied to the two rods directly below the trap center to counterbalance the

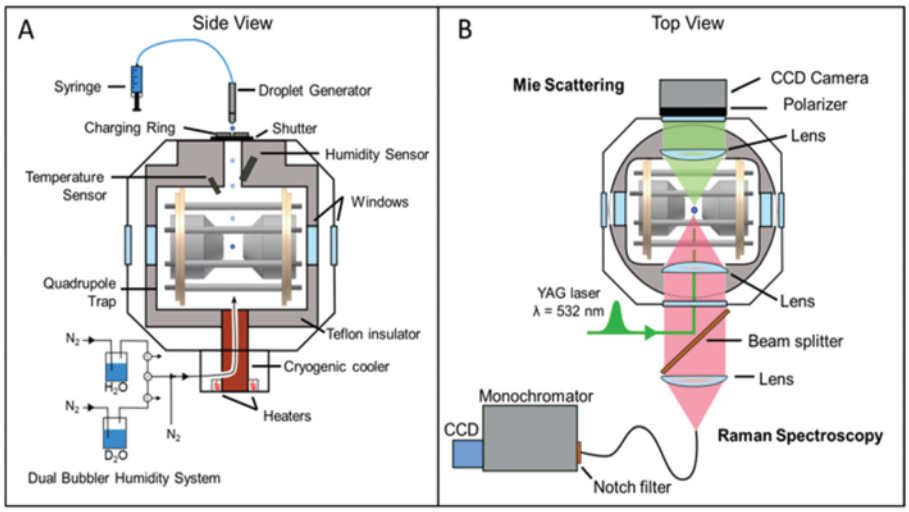

Fig. 1 (A) Experimental setup of the electrodynamic balance (EDB) apparatus contained in a secondary Teflon housing inside an environmental chamber and equipped with a droplet generator and dual bubbler RH control. (B) Optical layout for a trapped droplet irradiated using a pulsed 532 nm laser. The forward Mie elastic scattering is collected on a CCD camera and the back-scattered Raman signal is passed through a beamsplitter and focused into a monochromator.

gravitational force of the trapped microdroplet. The AC voltage is applied to the endcap electrodes only, at typical values of $V_p = 1500$ V and $f = 150$ Hz. During an experiment, the levitation voltage is adjusted using an automated LabView feedback control loop for maintaining the droplet in the trap center, while the AC frequency is maintained approximately constant.

The balance is mounted on a DN63CF Conflat flange equipped with electrical feedthroughs as well as a 1/8″ OD copper gas-line feedthrough for introducing humidified or dried nitrogen gas directly into the trap. The balance is constructed on two octagonal plates, and is isolated from air in the chamber by a set of stainless steel plates outfitted with windows, serving to electrically shield the high voltage electrodes that may otherwise interfere with the trajectory of incoming charged droplets. The plates also isolate air in the center of the balance from the surrounding chamber, reducing the surface area and thus the time for equilibration of the RH. The isolation of the balance is augmented by a secondary Teflon housing that provides a direct channel from the opening of the chamber. The droplet generator is located above the balance, allowing droplets to be injected directly into the trapping volume. An electronic shutter is located at the opening of the chamber that opens for the introduction of a new droplet. A piezoelectric droplet generator (Engineering Arts DE03) is connected to an electronic syringe pump for precise control of the production of the aqueous droplets. Filtered aqueous sucrose or CA solutions are aspirated into the capillary of the droplet generator from which single droplets approximately 40 μm in diameter are generated on demand using computer-controlled pulse generation to drive the piezoelectric element. A charging ring located above the shutter and electrically connected to the grounded piezoelectric tip inductively charges the droplets using an electrostatic potential. Occasionally, multiple droplets are trapped simultaneously and the frequency of the AC is adjusted until all but one droplets are ejected.

The relative humidity in the balance is controlled using digital mass flow controllers (Alicat MC-500SCCM) by mixing N_2 with the humidified vapor headspace of a bubbler containing water. Humidified nitrogen is subsequently directed through copper tubing wrapped around and welded to a copper standoff in thermal contact with a Stirling free-piston coldhead cooler (Sunpower Cryotel CT) and resistive heaters, which serve to maintain a constant temperature and thermalize the air before entering the trap. However, the temperature control was not used in these experiments and the trap was maintained at the laboratory temperature, approximately 20–23 °C. The temperature is recorded using a temperature probe (Vaisala HMP60) with ±1 °C accuracy. Two bubblers, one containing distilled H_2O and the other containing high purity D_2O (>99.8% D atom, Acros Organics), are arranged using 3-way valves as shown in Fig. 1A so that air from one bubbler is selected to flow into the chamber while the other bubbler is exhausted. Experiments are carried out at constant RH by first trapping a single sucrose or CA droplet in H_2O and allowing sufficient time for equilibration. Then, D_2O vapor at the same RH is introduced to the chamber, replacing the gas-phase H_2O in the balance and eventually diffusing into the H_2O droplet. During each experimental run, the H_2O humidified air is initially directed into the chamber for droplet equilibration while the D_2O bubbler is exhausted to fill intermediate tubing lines, minimizing changes in RH during the gas transition in the trap. The relative humidity and temperature are monitored using a humidity probe (Vaisala HMP60) with ±3% RH accuracy located approximately 25 mm downstream of the RH flow. For each water diffusion measurement, the relative humidity is maintained constant to ±1%, or within the error of the probe. When the chamber atmosphere is switched to D_2O, the humidity probe measurement must be corrected for the difference in equilibrium vapor pressure of D_2O *versus* H_2O,[41] as shown in eqn (1), where $A = -0.30661$, $B = 9.14056$, and

$C = 75.753$ and T is in Celsius.

$$\ln\left(\frac{p^0_{H_2O}}{p^0_{D_2O}}\right) = A + \frac{B}{C+T} \quad (1)$$

Two spectroscopic methods are used to characterize a trapped particle: Mie scattering for determining the particle size and Raman spectroscopy for chemical analysis. As shown in Fig. 1B, the trapped droplet is irradiated using a focused 80 kHz, 532 nm Nd:YAG laser beam (RPMC Wedge XF). The elastic Mie scattering is collimated using an *f*/2 lens with a solid angle of 24.5° centered at 45° in the forward-scattering direction and imaged onto a monochromatic CCD camera. The morphology of the trapped droplet is determined by the Mie scattering pattern. Spherical droplets exhibit evenly spaced bands and crystalline or amorphous solid particles exhibit an irregular pattern.[33] Fig. 2 shows an example Mie image of a single droplet and the resulting angular intensity spectrum, previously demonstrated in the literature to follow closely with Mie theory.[24] The diameter of droplets in these experiments is significantly larger than the wavelength of light, allowing a geometric optics approximation to be applied. The intensity spectrum is processed using a fast Fourier Transform (FFT) to compute an average band spacing, $\Delta\theta$, (rad^{-1}). The band spacing is used in conjunction with the index of refraction, n, to calculate the particle radius, r, using eqn (2):[42]

$$r = \frac{\lambda}{\Delta\theta}\left(\cos\left(\frac{\theta}{2}\right) + \frac{n\sin\left(\frac{\theta}{2}\right)}{\sqrt{1+n^2-2n\cos\left(\frac{\theta}{2}\right)}}\right)^{-1} \quad (2)$$

where λ is the laser wavelength (μm) and θ is the median scattering angle (rad). The parameterization of the index of refraction with concentration of sucrose is described further in the Results section.

The evolving chemical composition of the trapped droplet from H_2O to D_2O is analyzed using the intensity of the stretches ν(O–D) ~ 2500 cm^{-1} and ν(O–H) ~ 3400 cm^{-1} in the Raman spectrum. A representative Raman spectrum for a sucrose droplet is shown in Fig. 2, and a representative spectrum for a CA droplet is shown in the ESI,† in Fig. S3. The integrated intensity of the O–H and O–D stretch features allows calculation of the fractional concentration of D_2O in the droplet over time. The back-scattered Raman signal is collected using *f*/2 optics, transmitted through the 532 nm laser edge beam splitter, and focused into a fiber optic cable coupled into a monochromator (Acton SpectraPro 275) with an open-electrode TE-cooled CCD detector (Horiba Syncerity). The spectrometer is equipped with a 600 g mm^{-1} grating with a 750 nm blaze for optimized quantum efficiency between 620 and 660 nm. The integration time for each spectrum is 30–120 s to achieve an adequate signal-to-noise ratio. The LabView control and data acquisition program records the Mie and Raman spectra at a designated interval along with trap settings and conditions.

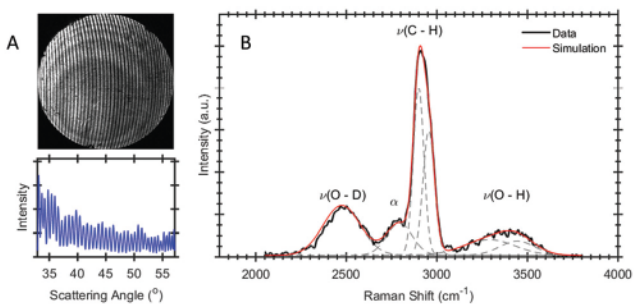

Fig. 2 (A) Mie scattering image collected on a CCD camera for a 54 μm sucrose droplet and the associated angular intensity spectrum used to calculate the droplet size. (B) Representative Raman spectrum for a sucrose droplet undergoing isotope exchange contains overlapping vibrational peaks that are simulated with a series of Gaussian peaks shown as the sum (red) and individual peak contributions (grey dashed).

3 Results and discussion

In this work, the time-dependent intensity of the ν(O–D) Raman peak is modeled using Fick's second law of diffusion to calculate the water diffusion coefficient in sucrose and CA microdroplets for a range of RH. The timescale for diffusion is highly dependent on the droplet radius and therefore an accurate size measurement is necessary for incorporation into the diffusion model. In order to calculate the droplet size using the angular intensity spectrum produced by the Mie scattering, the index of refraction was calculated as a function of sucrose or CA concentration, which varies with water activity or RH. The method of parameterization of the index of refraction will be presented, followed by a discussion of how the Raman spectra were analyzed to determine the rate of isotopic substitution as D_2O diffused into the suspended droplet. With these results, the solute-concentration-dependent water diffusion coefficients were calculated and modeled using a Vignes-type fit for comparison with the literature and validation of this method.

Parameterizations of the index of refraction

Calculation of the index of refraction for the droplet as a function of varying RH requires parameterization of the mass fraction solute (MFS) and density (ρ). The dependence of MFS on water activity, a_w, has been well studied for sucrose solutions and the treatment by Norrish[43] has been shown to correlate with experimental measurements over the entire RH range:

$$a_w = x_w \exp\left(k x_s^2\right) \quad (3)$$

where x_w and x_s are the mole fractions of water and the solute, respectively, and k is an empirical constant equal to −6.47 for sucrose.[44] While other parameterizations have been proposed,[38,45] the Norrish parametrization was shown to be most appropriate for sucrose solutions over a wide range of RH.[16,28] The density of a sucrose–water mixture can be taken as the volume additivity of pure component densities (VAD), with the pure component density of water, $\rho_w = 1000$ kg m^{-3}, and sucrose,[44] $\rho_s = 1580.5$ kg m^{-3} giving:

$$\frac{1}{\rho} = \frac{1-\mathrm{MFS}}{\rho_w} + \frac{\mathrm{MFS}}{\rho_s} \quad (4)$$

The refractive index of a sucrose solution varies with MFS and is parameterized using a linear fit with the refractive index for water, n = 1.33, at MFS(0) and n = 1.558 at MFS(1).[46] The calculated index of refraction of the sucrose droplet at a given RH is then used in eqn (2) to calculate the droplet diameter. The uncertainty in droplet size (±10 nm) due to wavelength-dependent dispersion is negligible compared to the experimental error (±500 nm) from the RH probe,[8] making it unnecessary to implement the highly accurate parameterization for sucrose solutions reported by Rosenbruch *et al.*[47] For CA, comprehensive parametrization of MFS with a_w and the refractive index of CA solution by Lienhard *et al.* was adopted.[48]

Diffusion of D_2O using Raman spectroscopy

The coefficient for translational diffusion of water, D_w, as a function of water activity, or RH, is extracted using a solution to Fick's second law of diffusion as applied to a sphere.[49] Considering sucrose, since the total amount of sucrose is constant throughout each experiment, all spectra are normalized to the sucrose ν(C–H) peak at 2930 cm^{-1}, allowing for correction for fluctuations in spectral intensity due to low amplitude motions of the droplet in the laser beam. A seven-Gaussian fit is applied to the spectrum between 2000 and 3800 cm^{-1} to determine individual peak contributions and therefore calculations of relative abundances of chemical species present. One Gaussian contributes to the O–D band, two Gaussians contribute to the C–H stretch, one Gaussian contributes to the weak C–H overtone peak (α), two Gaussians contribute to the O–H band, and a weak, broad Gaussian accounts for the background signal. Fig. 2B shows the contributions of the seven Gaussians, for example, in the Raman spectra of a sucrose droplet approximately halfway through an isotope exchange experiment when distinct peaks associated with both H_2O and D_2O are present.

In the case of CA droplets, 8 Gaussians are used to fit the spectra. The values of the fit parameters are adjusted relative to sucrose due to the distinct Raman spectra. Typical fit parameters are given in the ESI.† Three Gaussians are assigned to the O–D and O–H band each and two Gaussians represent C–H stretch peaks. For the spectra of the CA droplets, overall broadening of O–D and O–H stretch bands was observed and the α peak was found to be negligible compared to the sucrose droplets. We note that multiple Gaussians for fitting the O–H/O–D bands are necessary, because of the multiple configurations of the hydrogen bond network in liquid water.[50] Typical CA spectra and examples of the Gaussian fitting parameters for CA droplets are presented in the ESI.†

At a constant relative humidity, the total amount of water in the droplet is assumed to be constant and equal to the sum of the contributions from H_2O and D_2O. Fig. 3A shows the progression of Raman spectra collected during an experiment, starting from the top where only ν(O–H) is observed and over time, the intensity of ν(O–H) decays and ν(O–D) appears. The spectrum is decomposed using a multiple Gaussian peak fitting as discussed earlier, from which the peak areas for O–D and O–H are used to calculate the fractional concentration of D_2O in the droplet:

$$\phi_{OD} = \frac{A_{OD}}{A_{OD} + \frac{1}{\sqrt{2}}A_{OH}} \quad (5)$$

where the O–D stretch located at 2500 cm^{-1} has a lower integrated intensity by a factor of $1/\sqrt{2}$ based on the difference in reduced mass.[21] When the gas manifold valves are rotated to switch from H_2O to D_2O, there is a time delay until the chamber is sufficiently filled with D_2O and the isotope exchange begins. Fig. 3B shows the concentration fractions of D_2O and H_2O at 44% RH that are initially constant as the droplet equilibrates and then abruptly change from baseline values. It can be assumed that for a period of time, approximately 30–480 s over the RH range from 54% to 7%, respectively, the droplet is undergoing isotope exchange while the chamber atmosphere is

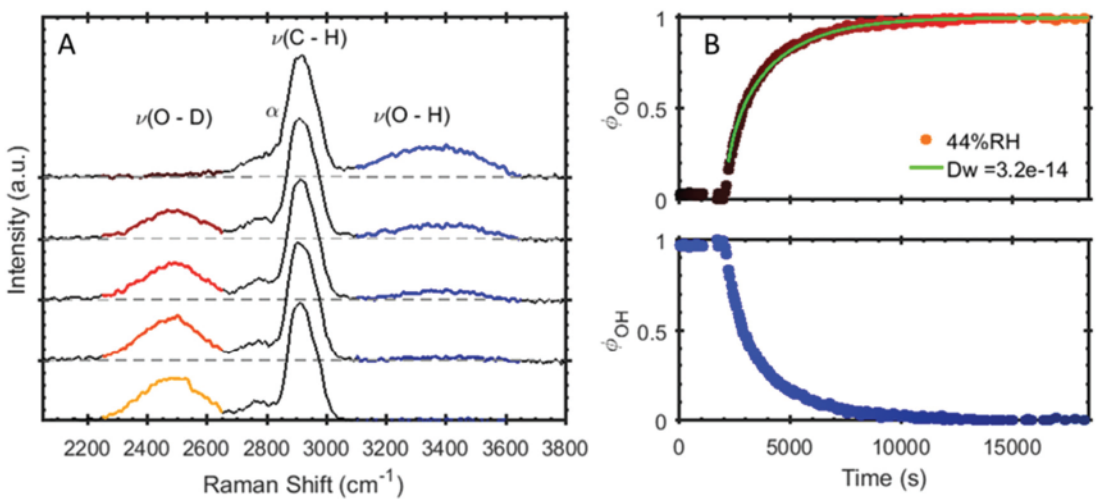

Fig. 3 (A) An example set of Raman spectra for a 54 μm sucrose droplet undergoing isotope exchange at 44% RH shows the decrease in peak intensity of ν(O–H) at ~3400 cm^{-1} and the growth of ν(O–D) at ~2500 cm^{-1}. (B) The fraction of water concentration of D_2O and H_2O in the droplet over time is modeled with Fickian diffusion to determine the concentration-dependent water diffusion coefficient.

a mixture of H_2O, HOD, and D_2O. Formation of HOD in a H_2O/D_2O mixture does not cause any detectable peak shift, and intensity changes from spectral features for the pure D_2O/H_2O mixture, *e.g.*, the spectral peak intensity of 50/50 H_2O/D_2O (that is composed of 25% H_2O, 25% D_2O and 50% HOD), agree with theoretical spectral features composed of 50% H_2O and 50% D_2O, confirming that a method based on eqn (5) is still valid to determine the original fractional concentration of D_2O.[50] During this time, the vapor–liquid interface does not meet the condition that the gas-phase concentration of D_2O is constant, assumed by the diffusion model derived from Fick's second law. In addition, we have neglected the difference in diffusion coefficients as H_2O and D_2O are assumed to have identical physical properties, within the reported error.[49] We therefore introduce a systematic approach for determining when constant D_2O RH is reached by fitting the time-dependent fractional concentration of OD with a three-parameter S-shaped curve where A, B, and C are empirically determined:

$$\phi_{OD} = \frac{1}{1 + A\exp(-B + Ct)} \quad (6)$$

The time at the inflection point of the S-shaped fit is selected as $t = 0$ for D_2O diffusion and indicates the time at which D_2O vapor has sufficiently replaced H_2O in the trapping volume, and only the successive O–D fractional concentration data (*e.g.*, the region where the green line spans Fig. 4b) are used in the calculations. The solution to Fick's second law of diffusion applied to a sphere is used to model the time-dependent dimensionless fractional concentration of the diffusing D_2O:[28,49]

$$\phi_{D_2O} = 1 - \left(\frac{6}{\pi^2}\right)\sum_{n=1}^{\infty}\frac{1}{n^2}\exp\left(-\frac{n^2\pi^2 D_w t}{a^2}\right) \quad (7)$$

where a is the particle radius and D_w is the translational diffusion constant. A three-term expansion of eqn (7) using a single adjustable parameter is used to calculate D_w for each of the experimental runs at a different RH. The upper limit for diffusion coefficients measured using this technique is calculated as $\sim 5 \times 10^{-13}$ m^2 s^{-1}. The sources of the upper limit include the rapid diffusion in the droplet sizes at high RH, the acquisition time required for adequate spectral signal-to-noise, and the time delay associated with fully replacing the composition of the atmosphere in the trapping volume.[28]

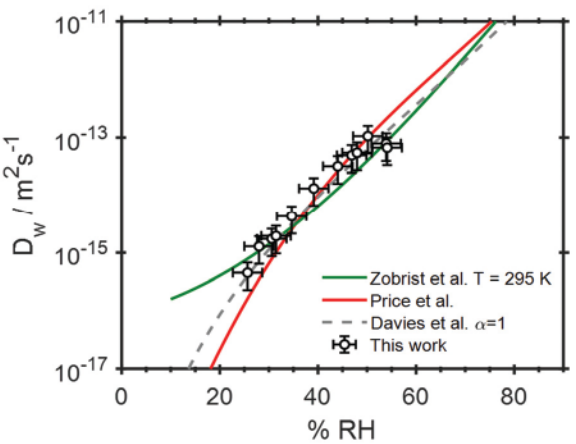

Fig. 4 Calculated water diffusion coefficients in sucrose droplets at varying RH studied in this work compared with parameterizations provided by Zobrist *et al.*,[38] Price *et al.*[21] and Davies *et al.*[28]

Water diffusion in aqueous sucrose droplets

The water diffusion coefficients measured for sucrose–water droplets at RH between 26 and 54% at room temperature are shown in Fig. 4. The RH is reported with the absolute error of the probe, ±3%, and the error in the D_w measurement is estimated as 50%, calculated from an uncertainty of ±20% in the model fit, ±1 μm uncertainty in the size calculation, differences in self-diffusion between H_2O and D_2O (10–24%),[21] the RH fluctuation (±1%) and temperature stabilization (±1 °C) over the course of an experiment. The results are compared with parameterizations from the literature reported by Zobrist *et al.*,[38] Price *et al.*,[21] and Davies *et al.*[28] Over the range where data were obtained, the results agree well with the Vignes-type parameterization that describes the variation of the water diffusion coefficient, D_w, with composition in a binary mixture:[51]

$$D_w = \left(D^0_{w,w}\right)^{x_w}\left(D^0_{w,s}\right)^{(1-x_w)}, \quad (8)$$

where x_w is the mole fraction of water, $D^0_{w,w}$ is the translational diffusion coefficient in pure water (2×10^{-9} m^2 s^{-1}), and $D^0_{w,s}$ is the self-diffusion coefficient of water in pure solute (1.9×10^{-27} m^2 s^{-1}, reported by Davies *et al.*[28]). Excellent agreement was found between the present results using the EDB and previous reports using various techniques,[28,52,53] showing the viability of this method for quantifying the translational diffusion coefficient over a range of water activities. However, the agreement deviates when approaching the high RH limit. At 54%, the timescale for diffusion is comparable to the turnover time for replacing the air in the chamber, allowing for isotopic exchange to occur rapidly in the droplet while exposed to an effectively lower D_2O concentration because the air is still a mixture of H_2O and D_2O. The resulting D_w at high RH, approximately 1×10^{-13} m^2 s^{-1}, is lower than the Vignes-type trend followed by other published results and serves as an upper bound to the dynamic range of the diffusion coefficients that can be quantified using this experimental setup.

The results in Fig. 4 are consistent with measurements carried out using isotope exchange on 6–300 μm diameter samples, which suggests that there is not a significant impact of droplet size on the water diffusion coefficient in the 35–60 μm size range studied. The droplet diameters studied in this work were significantly larger than the <10 μm diameter droplets used by Zobrist *et al.*[38] and Davies *et al.*[28] and significantly smaller than the 200–300 μm diameter substrate-supported disks used by Price *et al.*[21] This suggests that the droplet size does not have a significant effect on the diffusion coefficient as a correlation between D_w and diameter across these different size ranges is not observed. The D_w of sucrose solution below 25% RH is of great interest because prediction using two methods (isotope exchange and mass transport)

diverges by orders of magnitude. The large discrepancy is due to different assumptions used in the two models. In the mass transport model, the radius of the droplet changes as it experiences sorption and desorption of water with the RH change. On the other hand, the isotope exchange model assumes a constant radius of the droplet held at fixed RH. Thus, the mass transport model involves a moving and non-linear boundary condition while the isotope exchange model assumes a fixed linear boundary condition.[49,52] Measuring D_w at RH below 25% in the case of sucrose was beyond the scope of the current measurements due to the diffusion timescales.[54,55]

The present results can be compared with both charge-neutral particles in the case of the isotope-exchange measurements of Price *et al.*[21] and Davies *et al.*[28] and charged particles in the mass-transport measurements of Zobrist *et al.*[38] The comparison suggests that the surface charge density on the droplets in this work (<40 elementary charges per μm^2) does not significantly influence D_2O diffusion into droplets. If the charge state significantly impacted the diffusion of D_2O into the droplet, the best agreement would be expected between the results conducted in EDBs, which is not the case. Instead, the best agreement was found with the optical tweezer measurements on neutral microdroplets using the isotope labeling technique. These results can be understood in the context of studies on the influence of charge on both ice nucleation and efflorescence. Homogeneous ice nucleation rates of pure water droplets were measured in a temperature-controlled EDB as a function of temperature and absolute charge and it was concluded that while temperature strongly influenced the nucleation rate, no correlation with the surface charge was observed over a range of ±200 charges per μm^2.[34,56] Charged droplets with 10× greater surface charge density compared to the droplets in the current work were examined and no effect of the charge on nucleation was found, supporting the conclusion that excess charges are not interfering with bulk processes such as diffusion within a droplet. Another recent study measured the dependence of the efflorescence relative humidity on the magnitude of the surface charge in sodium chloride microdroplets and found no correlation below 500 elementary charges per μm^2.[37] Molecular dynamics simulations showed that above this charge density threshold, the charges interact with dissolved ionic species to form stable critical cluster sizes necessary for overcoming the energetic nucleation barrier at higher RH compared to neutral droplets. In the present work, the sucrose droplets contain surface charge density significantly below the threshold suggested by Hermann *et al.*[37] to impact efflorescence behavior. Thus, the present work demonstrates an alternative way that can be used to study particles incompatible with optical trapping techniques, *e.g.*, amorphous (or glassy) aerosols or solid particles that have non-spherical morphology.

Water diffusion in aqueous citric acid droplets

Water diffusion in citric acid solution droplets was measured over a lower RH range (7–25%) compared to sucrose. The RH-dependent refractive index of a CA solution was parameterized using the MFS of CA and water to deduce the droplet size.[48] The RH dependent D_w values of CA droplets are shown in Fig. 5, revealing good agreement with the other isotope exchange measurements using optical tweezers[28] and a significant deviation from D_w values measured by mass-transfer[57] as well as the predictions of the S–E equation.[58] Isotope-exchange derived D_w values of CA below 10% RH at room temperature are reported here for the first time, and it is found that in this regime, the intensity of the Raman O–H band at 3400 cm^{-1} does not diminish to zero in the exchange process. This may arise from inhibited diffusion of water in CA droplets under very dry conditions. In addition, the results at RH lower than 15% reveal that the aqueous CA droplets do not undergo full isotope exchange, with all labile hydrogens replaced by deuterium, over a period up to 65 hours. This observation may be a result of the much larger size of the droplet compared to the study of Davies and Wilson.[28] Because eqn (7) assumes complete H_2O/D_2O exchange, it is no longer valid for describing water diffusion at RH < 15%. To analyze incomplete H_2O/D_2O exchange for CA at lower RHs, we introduce a modified solution to Fick's 2nd law, eqn (9). The equation contains an additional parameter χ that represents the fractional exchange as a function of RH, and reveals the kinetic limitation of water diffusion. For instance, $\chi = 1$ means complete exchange of H_2O to D_2O and eqn (9) is analogous to eqn (7), while $\chi = 0.7$ indicates that 70% of the total H_2O in the droplet is exchanged to D_2O.

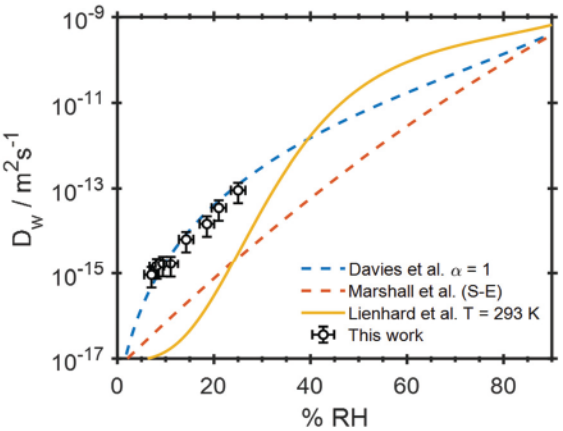

Fig. 5 RH dependent D_w for CA droplets compared to other experiments. Isotopic exchange using optical tweezers (Davies *et al.*),[28] mass transfer (Lienhard *et al.*),[52] and S–E prediction using viscosity data (Marshall *et al.*).[53]

$$\phi_{D_2O} = \chi\left(1 - \left(\frac{6}{\pi^2}\right)\sum_{n=1}^{\infty}\frac{1}{n^2}\exp\left(-\frac{n^2\pi^2 D_w t}{a^2}\right)\right) \quad (9)$$

Application of the two eqn (7) and (9) to the isotope exchange data at low RH is illustrated in ESI,† Fig. S5, showing that eqn (9) represents the physical phenomena significantly better than eqn (7). Fig. 6 shows the strong observed dependence of χ on RH, illustrating the incomplete H_2O/D_2O exchange at lower RH ($\chi < 1$) and full exchange of H_2O to D_2O at RH higher than 15% ($\chi \sim 1$). It is not surprising for CA droplets of this size to develop a radial concentration gradient

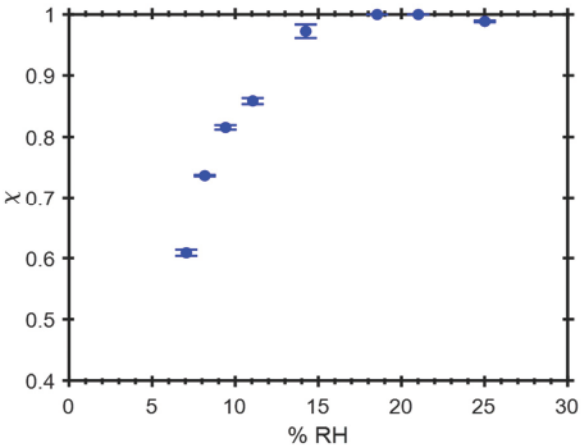

Fig. 6 Kinetic limitations of water diffusion are evident at RH below 15% shown as nonunity ϕ_{D_2O} values given by eqn (9). Error bars represent the 95% confidence interval of the fitting parameter χ.

under dry conditions. Consequently, the true values of D_w are expected to be smaller than the values calculated using eqn (9) because the diffusion of D_2O into the droplet core is not complete. The Fickian diffusion model assumes a homogeneous mixture after sufficient equilibration time, which is not truly achieved here owing to the kinetic limitation, but it was chosen for the analysis of D_w in the CA droplets as well owing to its simplicity and applicability to both sucrose and CA data. A kinetic multi-layer model[59] or Maxwell–Stefan diffusion model[60] may be used in future studies to describe the formation of the concentration gradient within the droplet as these models explicitly consider the droplet as a series of spherical shells.

Similar kinetic limitations of diffusion have previously been observed for ambient organic aerosols, particularly in highly viscous or glassy state aerosols where formation of a significant radial concentration gradient in the droplet inhibits reaching thermodynamic equilibrium.[1,61] The inhibited diffusion of water in CA droplets may be attributed to the formation of molecular clusters in the supersaturated solution. It is worth comparing the results of H_2O/D_2O exchange at the lower RH bound for sucrose (26%) and CA (7%). The exchange was incomplete for CA over several days while sucrose showed full exchange ($\chi = 1$) even though the D_w value of CA (9.19×10^{-16} m^2 s^{-1}) is notably higher than that of sucrose (4.52×10^{-16} m^2 s^{-1}) under the stated conditions. In addition, the viscosities of the droplets show orders of magnitude difference ($\sim 10^{10}$ Pa s for sucrose *vs.* $\sim 10^4$ Pa s for CA). Taking these observations into account, one can suppose that CA has a much higher propensity to form organized molecular structures with water than sucrose does within the highly-saturated solution (MFS $>$ 0.9). This is supported by studies that observed solute clustering in supersaturated CA solutions.[62–65] From a chemical perspective, citric acid is a tricarboxylic acid that will have much stronger interactions with water through the acidic hydrogens and the polar –COOH groups compared to sucrose. Similar kinetic inhibition of diffusion of reactive condensed-phase species has been reported for glassy aerosols at low RH[8,9,57] but our result explicitly shows the strong dependence of this phenomenon on RH. Aggregation of solute–water clusters in supersaturated droplets may lead to radial concentration gradients that promote the formation of a core–shell morphology, preserving the unreacted core species with potential implications for surface-sensitive phenomena such as cloud condensation nucleation (CCN) and ice nucleation (IN) activities.[66] Mie scattering measurements remained consistent with liquid droplets even at these low RHs, so the question that arises is how 'liquid' or 'solid' a particle needs to be to distinguish the particle phase by Mie scattering.[67,68]

4 Conclusions

The translational water diffusion coefficient was measured in single charged sucrose and CA droplets as a model system for sea spray aerosols at humidities ranging from 26–54% RH for sucrose and 7–25% RH for CA at room temperature. Water diffusion has been quantified using H_2O/D_2O isotope tracing measured *via* Raman spectroscopy of a single charged droplet trapped in a humidity-controlled EDB. The measured water diffusion coefficient–molar concentration relationship follows an exponential dependence, described as a Vignes-type parameterization. The data were compared with previous studies of the sucrose–water and CA–water systems using the isotope exchange technique on neutral samples and a mass transport method on charged droplets. The comparison between our results and those of other Raman spectroscopy based methods shows a good agreement of water diffusion coefficients across a wide range of sample sizes and volumes, suggesting that the D_w values are not size-dependent. The agreement of this work using charged droplets in an EDB with neutral particles in an optical trap suggests that charge does not play a significant role under the conditions studied.

The Raman spectroscopic technique for isotope exchange analysis is limited to particle sizes greater than 1 μm because of the low signal to noise ratio. Improvement in the sensitivity of the optical setup would be of great value in extending the present measurements to smaller aerosols with diameters of 50–200 nm, which are the size population most efficient for cloud activation[69,70] and therefore of large climate relevance. Experimental modifications to control temperature and particle charge will reduce uncertainties in the diffusion measurements and allow a more detailed examination of charge effects. Temperature control will also enable further comparisons of the method over a range of atmospherically relevant temperatures with the temperature-dependent D_w measurements made using the mass transport method,[38] as well as extending these measurements to examine the effect of viscosity and chemical composition on ice nucleation.

The present measurements further demonstrate the ability to measure water diffusion independently from viscosity under atmospherically relevant conditions. The isotope exchange method for measuring water diffusion rates can be applied to a variety of chemical systems and complexity including ternary mixtures of atmospheric relevance, the influence of hygroscopic

inorganic salts, and concentration-dependent effects of monovalent and divalent cations found in sea spray aerosols. One of the first systems to investigate at reduced temperatures will be the citric acid system to examine further the origin of the strong kinetic limitation to isotope exchange.

Conflicts of interest

There are no conflicts to declare.

Acknowledgements

This work was supported by the NSF through the NSF Center for Aerosol Impacts on Chemistry of the Environment (CAICE), CHE-1801971. We thank J. Mayer for his contributions to apparatus design and fabrication. We also thank the reviewers for insightful comments. All relevant data will be made available online at the CAICE digital collection at the UC San Diego library (https://library.ucsd.edu/dc/collection/bb96275693).

References

1 B. Zobrist, C. Marcolli, D. A. Pedernera and T. Koop, *Atmos. Chem. Phys.*, 2008, **8**, 5221–5244.
2 M. V. Orellana, P. A. Matrai, C. Leck, C. D. Rauschenberg, A. M. Lee and E. Coz, *Proc. Natl. Acad. Sci. U. S. A.*, 2011, **108**, 13612–13617.
3 A. Virtanen, J. Joutsensaari, T. Koop, J. Kannosto, P. Yli-Pirila, J. Leskinen, J. M. Makela, J. K. Holopainen, U. Poschl, M. Kulmala, D. R. Worsnop and A. Laaksonen, *Nature*, 2010, **467**, 824–827.
4 E. Jarvinen, K. Ignatius, L. Nichman, T. B. Kristensen, C. Fuchs, C. R. Hoyle, N. Hoppel, J. C. Corbin, J. Craven, J. Duplissy, S. Ehrhart, I. El Haddad, C. Frege, H. Gordon, T. Jokinen, P. Kallinger, J. Kirkby, A. Kiselev, K. H. Naumann, T. Petaja, T. Pinterich, A. S. H. Prevot, H. Saathoff, T. Schiebel, K. Sengupta, M. Simon, J. G. Slowik, J. Trostl, A. Virtanen, P. Vochezer, S. Vogt, A. C. Wagner, R. Wagner, C. Williamson, P. M. Winkler, C. Yan, U. Baltensperger, N. M. Donahue, R. C. Flagan, M. Gallagher, A. Hansel, M. Kulmala, F. Stratmann, D. R. Worsnop, O. Mohler, T. Leisner and M. Schnaiter, *Atmos. Chem. Phys.*, 2016, **16**, 4423–4438.
5 M. Shiraiwa and J. H. Seinfeld, *Geophys. Res. Lett.*, 2012, **39**, L24801.
6 J. F. Davies and K. R. Wilson, *Chem. Sci.*, 2015, **6**, 7020–7027.
7 P. F. Liu, Y. J. Li, Y. Wang, A. P. Bateman, Y. Zhang, Z. H. Gong, A. K. Bertram and S. T. Martin, *ACS Cent. Sci.*, 2018, **4**, 207–215.
8 H. J. Tong, J. P. Reid, D. L. Bones, B. P. Luo and U. K. Krieger, *Atmos. Chem. Phys.*, 2011, **11**, 4739–4754.
9 D. L. Bones, J. P. Reid, D. M. Lienhard and U. K. Krieger, *Proc. Natl. Acad. Sci. U. S. A.*, 2012, **109**, 11613–11618.
10 J. W. Lu, A. M. J. Rickards, J. S. Walker, K. J. Knox, R. E. H. Miles, J. P. Reid and R. Signorell, *Phys. Chem. Chem. Phys.*, 2014, **16**, 9819–9830.
11 D. M. Lienhard, A. J. Huisman, U. K. Krieger, Y. Rudich, C. Marcolli, B. P. Luo, D. L. Bones, J. P. Reid, A. T. Lambe, M. R. Canagaratna, P. Davidovits, T. B. Onasch, D. R. Worsnop, S. S. Steimer, T. Koop and T. Peter, *Atmos. Chem. Phys.*, 2015, **15**, 13599–13613.
12 K. Ignatius, T. B. Kristensen, E. Jarvinen, L. Nichman, C. Fuchs, H. Gordon, P. Herenz, C. R. Hoyle, J. Duplissy, S. Garimella, A. Dias, C. Frege, N. Hoppel, J. Troestl, R. Wagner, C. Yan, A. Amorim, U. Baltensperger, J. Curtius, N. M. Donahue, M. W. Gallagher, J. Kirkby, M. Kulmala, O. Mohler, H. Saathoff, M. Schnaiter, A. Tome, A. Virtanen, D. Worsnop and F. Stratmann, *Atmos. Chem. Phys.*, 2016, **16**, 6495–6509.
13 J. W. Grayson, M. Song, M. Sellier and A. K. Bertram, *Atmos. Meas. Tech.*, 2015, **8**, 2463–2472.
14 L. Renbaum-Wolff, J. W. Grayson and A. K. Bertram, *Atmos. Chem. Phys.*, 2013, **13**, 791–802.
15 Y. C. Song, A. E. Haddrell, B. R. Bzdek, J. P. Reid, T. Barman, D. O. Topping, C. Percival and C. Cai, *J. Phys. Chem. A*, 2016, **120**, 8123–8137.
16 R. M. Power, S. H. Simpson, J. P. Reid and A. J. Hudson, *Chem. Sci.*, 2013, **4**, 2597–2604.
17 C. D. O'Dowd, M. C. Facchini, F. Cavalli, D. Ceburnis, M. Mircea, S. Decesari, S. Fuzzi, J. Y. Young and J. P. Putaud, *Nature*, 2004, **431**, 676–680.
18 S. K. Kumar, G. Szamel and J. F. Douglas, *J. Chem. Phys.*, 2006, **124**, 214501.
19 V. Molinero and W. A. Goddard, *Phys. Rev. Lett.*, 2005, **95**, 045701.
20 L. Zhu, T. Cai, J. Huang, T. C. Stringfellow, M. Wall and L. Yu, *J. Phys. Chem. B*, 2011, **115**, 5849–5855.
21 H. C. Price, B. J. Murray, J. Mattsson, D. O'Sullivan, T. W. Wilson, K. J. Baustian and L. G. Benning, *Atmos. Chem. Phys.*, 2014, **14**, 3817–3830.
22 R. J. Hopkins, L. Mitchem, A. D. Ward and J. P. Reid, *Phys. Chem. Chem. Phys.*, 2004, **6**, 4924–4927.
23 P. Chylek, V. Ramaswamy, A. Ashkin and J. M. Dziedzic, *Appl. Opt.*, 1983, **22**, 2302–2307.
24 A. K. Ray, A. Souyri, E. J. Davis and T. M. Allen, *Appl. Opt.*, 1991, **30**, 3974–3983.
25 B. J. Dennis-Smither, R. E. H. Miles and J. P. Reid, *J. Geophys. Res.*, 2012, **117**, D20204.
26 B. J. Dennis-Smither, F. H. Marshall, R. E. H. Miles, T. C. Preston and J. P. Reid, *J. Phys. Chem. A*, 2014, **118**, 5680–5691.
27 C. Cai, D. J. Stewart, J. P. Reid, Y. H. Zhang, P. Ohm, C. S. Dutcher and S. L. Clegg, *J. Phys. Chem. A*, 2015, **119**, 704–718.
28 J. F. Davies and K. R. Wilson, *Anal. Chem.*, 2016, **88**, 2361–2366.
29 J. F. Davies, A. E. Haddrell and J. P. Reid, *Aerosol Sci. Technol.*, 2012, **46**, 666–677.
30 J. F. Davies, R. E. H. Miles, A. E. Haddrell and J. P. Reid, *Proc. Natl. Acad. Sci. U. S. A.*, 2013, **110**, 8807–8812.
31 R. E. H. Miles, J. F. Davies and J. P. Reid, *Phys. Chem. Chem. Phys.*, 2016, **18**, 19847–19858.
32 J. F. Davies, R. E. H. Miles, A. E. Haddrell and J. P. Reid, *J. Geophys. Res.*, 2014, **119**, 10931–10940.

33 H. Vortisch, B. Kramer, I. Weidinger, L. Woste, T. Leisner, M. Schwell, H. Baumgartel and E. Ruhl, *Phys. Chem. Chem. Phys.*, 2000, **2**, 1407–1413.
34 B. Kramer, O. Hubner, H. Vortisch, L. Woste, T. Leisner, M. Schwell, E. Ruhl and H. Baumgartel, *J. Chem. Phys.*, 1999, **111**, 6521–6527.
35 P. Stockel, H. Vortisch, T. Leisner and H. Baumgartel, *J. Mol. Liq.*, 2002, **96–97**, 153–175.
36 H. J. Tong, B. Ouyang, N. Nikolovski, D. M. Lienhard, F. D. Pope and M. Kalberer, *Atmos. Meas. Tech.*, 2015, **8**, 1183–1195.
37 G. Hermann, Y. Zhang, B. Wassermann, H. Fischer, M. Quennet and E. Ruhl, *J. Phys. Chem. A*, 2017, **121**, 6790–6799.
38 B. Zobrist, V. Soonsin, B. P. Luo, U. K. Krieger, C. Marcolli, T. Peter and T. Koop, *Phys. Chem. Chem. Phys.*, 2011, **13**, 3514–3526.
39 S. Schlemmer, J. Illemann, S. Wellert and D. Gerlich, *J. Appl. Phys.*, 2001, **90**, 5410–5418.
40 A. J. Trevitt, P. J. Wearne and E. J. Bieske, *Int. J. Mass Spectrom.*, 2007, **262**, 241–246.
41 M. Salomon, *Thermodynamic Properties of Liquid H_2O and D_2O and Their Mixtures*, United States. National Aeronautics and Space Administration. "NASA Technical Note." Print., Washington, D.C., 1969.
42 W. J. Glantschnig and S. H. Chen, *Appl. Opt.*, 1981, **20**, 2499–2509.
43 R. S. Norrish, *J. Food Sci. Technol.*, 1966, **1**, 25–39.
44 J. Chirife, C. Ferro Fontan and E. A. Benmergui, *J. Food Technol.*, 1980, **15**, 59–70.
45 M. Starzak and S. D. Peacock, *Zuckerindustrie*, 1997, **122**, 380–387.
46 D. R. Lide, *CRC Handbook of Chemistry and Physics*, CRC Press Inc., Boca Raton, FL, 79th edn, 1998.
47 K. J. Rosenbruch, B. Prowe and H. Reuschel, *PTB-Mitt.*, 1975, **85**, 458–465.
48 D. M. Lienhard, D. L. Bones, A. Zuend, U. K. Krieger, J. P. Reid and T. Peter, *J. Phys. Chem. A*, 2012, **116**, 9954–9968.
49 A. Moridnejad and T. C. Preston, *J. Phys. Chem. A*, 2016, **120**, 9759–9766.
50 Q. Hu, H. Zhao and S. Ouyang, *Phys. Chem. Chem. Phys.*, 2017, **19**, 21540–21547.
51 A. Vignes, *Ind. Eng. Chem. Fundam.*, 1966, **5**, 189–199.
52 B. Zobrist, V. Soonsin, B. P. Luo, U. K. Krieger, C. Marcolli, T. Peter and T. Koop, *Phys. Chem. Chem. Phys.*, 2011, **13**, 3514–3526.
53 H. C. Price, J. Mattsson and B. J. Murray, *Phys. Chem. Chem. Phys.*, 2016, **18**, 19207–19216.
54 A. M. J. Rickards, Y. C. Song, R. E. H. Miles, T. C. Preston and J. P. Reid, *Phys. Chem. Chem. Phys.*, 2015, **17**, 10059–10073.
55 T. C. Preston and J. P. Reid, *J. Opt. Soc. Am. B*, 2013, **30**, 2113–2122.
56 D. Rzesanke, J. Nadolny, D. Duft, R. Muller, A. Kiselev and T. Leisner, *Phys. Chem. Chem. Phys.*, 2012, **14**, 9359–9363.
57 D. M. Lienhard, A. J. Huisman, D. L. Bones, Y. F. Te, B. P. Luo, U. K. Krieger and J. P. Reid, *Phys. Chem. Chem. Phys.*, 2014, **16**, 16677–16683.
58 F. H. Marshall, R. E. H. Miles, Y. C. Song, P. B. Ohm, R. M. Power, J. P. Reid and C. S. Dutcher, *Chem. Sci.*, 2016, **7**, 1298–1308.
59 M. Shiraiwa, C. Pfrang and U. Pöschl, *Atmos. Chem. Phys.*, 2010, **10**, 3673–3691.
60 K. Fowler, P. J. Connolly, D. O. Topping and S. O'Meara, *Atmos. Chem. Phys.*, 2018, **18**, 1629–1642.
61 A. Virtanen, J. Joutsensaari, T. Koop, J. Kannosto, P. Yli-Pirilä, J. Leskinen, J. M. Mäkelä, J. K. Holopainen, U. Pöschl, M. Kulmala, D. R. Worsnop and A. Laaksonen, *Nature*, 2010, **467**, 824–827.
62 J. W. Mullin and C. L. Leci, *Philos. Mag.*, 1969, **19**, 1075–1077.
63 K. Ohgaki, Y. Makihara, M. Morishita, M. Ueda and N. Hirokawa, *Chem. Eng. Sci.*, 1991, **46**, 3283–3287.
64 K. Ohgaki, N. Hirokawa and M. Ueda, *Chem. Eng. Sci.*, 1992, **47**, 1819–1823.
65 M. A. Larson and J. Garside, *Chem. Eng. Sci.*, 1986, **41**, 1285–1289.
66 M. Shiraiwa, Y. Li, A. P. Tsimpidi, V. A. Karydis, T. Berkemeier, S. N. Pandis, J. Lelieveld, T. Koop and U. Pöschl, *Nat. Commun.*, 2017, **8**, 1–7.
67 C. F. Bohren and D. R. Huffman, *Absorption and Scattering of Light by Small Particles*, 1998, vol. 31.
68 C. Mätzler, *IAP Research Report*, 2002, 2002–08, opening-18.
69 M. Komppula, H. Lihavainen, V. M. Kerminen, M. Kulmala and Y. Viisanen, *J. Geophys. Res.*, 2005, **110**, D06204.
70 H. C. Che, X. Y. Zhang, L. Zhang, Y. Q. Wang, Y. M. Zhang, X. J. Shen, Q. L. Ma, J. Y. Sun and J. T. Zhong, *Sci. Rep.*, 2017, **7**, 5819.